Composite Salt in Porous Metal-Organic Frameworks for Adsorption Heat Transformation

Luis Garzón-Tovar[†], Javier Pérez-Carvajal[†], Inhar Imaz[*†] and Daniel Maspoch*[*†‡]*

† Catalan Institute of Nanoscience and Nanotechnology (ICN2), CSIC and The Barcelona Institute of Science and Technology, Campus UAB, Bellaterra, 08193 Barcelona, Spain. E-mail: inhar.imaz@icn2.cat, daniel.maspoch@icn2.cat

‡ ICREA, Pg. Lluís Companys 23, 08010 Barcelona, Spain

ABSTRACT

Adsorptive heat transformation (AHT) systems such as adsorption thermal batteries and chillers can provide space heating and cooling in a more environmental friendly way. However, their use is still hindered by their relatively poor performances and large sizes due to the limited properties of solid adsorbents. Here, we report the spray-drying continuous-flow synthesis of a new type of solid adsorbents that results from combining metal-organic frameworks (MOFs), such as UiO-66, and hygroscopic salts, such as $CaCl_2$. These adsorbents, commonly named as composite salt in porous matrix (CSPM)

materials, are packed in the form of spherical superstructures/beads. In terms of water sorption properties, these composites allow improving the water uptake capabilities of MOFs while preventing their dissolution in the water adsorbed; a common characteristic of these salts due to the deliquescence effect. We anticipate that these MOF-based CSPMs, in which the percentage of salt can be tuned, are promising candidates for adsorption thermal batteries and chillers. In the first application, we show that a CSPM made of UiO-66 and $CaCl_2$ (38 % w/w) exhibits a heat storage capacity of 367 kJ kg^{-1}. For adsorption chillers, we demonstrate that a second CSPM made of UiO-66 and $CaCl_2$ (53 % w/w) shows a specific cooling power of 631 W kg^{-1} and a coefficient of performance of 0.83, comparable to the best solid adsorbents reported so far.

INTRODUCTION

The anthropogenic greenhouse gas emissions related to the demand of electrical energy by traditional space heating and air conditioning processes have increased over the past decade.[1] To solve this problem, several initiatives have been proposed to replace the traditional vapor compression devices by more environmentally friendly adsorptive heat transformation (AHT) systems, such as adsorption chillers, heat pumps and thermal batteries.[2] These AHT systems are based on an adsorption-desorption cycle of a working fluid, where useful heat is released during the adsorption step and cold is produced during the evaporation of the working fluid. The main advantages of these systems are (i) the possibility to use low thermal energy sources (*e.g.* solar and waste heat) for regeneration and driving energy; and (ii) that water can be used as the working fluid.[3]

Despite these advantages, the AHT technologies are not yet competitive with conventional vapour compression systems due to the low performance of the working pair (adsorbent-adsorbate); sometimes associated to the low adsorption capacity of the adsorbent.[4] In this sense, inorganic adsorbents such as LiCl and $CaCl_2$ salts have been widely explored.[5] These compounds can adsorb a large amount of water because of their hygroscopic capacity. However, the presence of deliquescence phenomena, which can cause corrosion problems and limit their water uptake, depresses their performance in real applications.[6] A solution that has been traditionally proposed is the use of porous materials for confining these inorganic compounds. In the resulting Composite Salt in Porous Matrix (CSPM), the porous matrix mainly acts as a media to disperse the salt particles and can provide good heat and mass transport to these salt particles.[5] These CSPMs are usually produced by impregnation and saturation methods,[4a] in which the inorganic solution is diffused into the porous matrix.[7] To date, different porous matrices have been explored for making CSPMs, including silica, filosilicates, activated carbon and microporous zeolites.[8] In an ideal material, however, the porous matrix also should adsorb water and provide efficient heat and mass transfer. In this context, silica-based and activated carbons generally display very low adsorption uptake in the range of P/P_0 = 0.3-0.5 due to its high hydrophobicity,[9] and zeolites achieve their maximum capacity at low relative pressures, but it is difficult to regenerate them due to the high desorption temperatures required (*e.g.* Zeolite-13X: 150 ºC; Zeolite-NaX: 360 ºC).[8a, 10]

Currently, the promising family of crystalline porous materials known as metal-organic frameworks (MOFs) has received great interest on water-sorption applications due to their high porosity, structural stability and tuneable composition (*e.g.* hydrophilic and hydrophobic moieties can co-exist in the same structure).[11] These potential applications

include heat transformation processes;[12] proton conductivity;[13] air dehumidification;[14] and water delivery in remote areas.[15] It is noticed that some MOFs have a high water adsorbent capacity (*e.g.* MIL-101(Cr)-NH_2: 1.05 g_{water} g^{-1}_{MOF}; MIL-100(Fe): 0.87 g_{water} g^{-1}_{MOF}; PIZOF-2 = 0.68 g_{water} g^{-1}_{MOF}),[2a, 12a] and that new strategies have started to be developed for improving these water adsorption capabilities. For example, Yan *et al*. have recently reported a new composite based on MIL-101 containing graphite oxide and exhibiting high water vapour capacity (maximum uptake up to 1.6 g_{water} $g^{-1}_{sorbent}$).[16] To the best of our knowledge, however, other MOF-based composites that enhance the water uptake and/or the use of MOFs as porous matrices to produce CSPMs have not been reported in the literature so far.

In this sense, we have recently reported that the spray drying method can be used to synthesize MOFs in the form of spherical hollow or compact superstructure/beads built up from the assembly of nanosized crystals.[17] An interesting feature of these superstructures is that their nitrogen adsorption isotherms at 77 K normally show a continuous increase of the N_2 uptake at partial pressures over 0.4, suggesting the presence of interparticular voids in the mesoporous range resulting from the assembly of MOF nanocrystals. Here, we take advantage of these voids and the inherent microporosity of MOFs to use these superstructures as porous matrices to confine inorganic salts. We show that this strategy is suitable to develop effective CSPMs based on MOFs for adsorption heat transformation. For synthesizing these CSPMs, we chose UiO-66 and UiO-66-NH_2 as the porous MOF matrices, and $CaCl_2$ and LiCl as the inorganic salts. We chose UiO-66 and UiO-66-NH_2 because of their high thermal and water stability and its water sorption capabilities.[18] And we chose $CaCl_2$ and LiCl because their excellent water uptake capabilities.

RESULTS AND DISCUSSION

Continuous-flow spray-drying synthesis

The composites were prepared by the spray-drying continuous-flow method, which enabled simultaneous synthesis and shaping of microspherical CSPMs made of $CaCl_2$ and UiO-66. In a typical experiment, a precursor solution containing $ZrCl_4$, 1,4-benzene dicarboxylic acid (BDC), $CaCl_2 \cdot 2H_2O$, H_2O and DMF in a molar ratio of 1:1:1.6:40:135 (concentration of $ZrCl_4$ = 0.1 M) was injected into the coil flow reactor at a feed rate of 2.4 mL·min^{-1} and at a T_1 of 115 ºC. The residence time inside the coil flow reactor was 63 s. The resulting pre-heated solution was then spray dried at a T_2 of 180 ºC and a flow rate of 336 mL min^{-1}, using a B-290 Mini Spray Dryer (BUCHI Labortechnik). Once the solution had atomized, a white powder was collected from the spray dryer collector. This powder was analyzed through Field-Emission Scanning Electron Microscopy (FESEM), which revealed the homogeneous formation of the characteristic spherical superstructures with an average size of 4.0 ± 1.9 μm (Figure 1a). X-ray powder diffraction (XRPD) confirmed the presence of both UiO-66 and $CaCl_2$ hydrates forming the superstructures (Figure 1b). The content of Ca in the composites was estimated by digesting this powder (previously outgassed at 200 ºC under vacuum) in H_2SO_4 at 50 ºC and analysed by ICP-OES, from which a $CaCl_2$ content of 38 % (hereafter, w_{CaCl_2}/w_{CSPM}) in the composite (hereafter, $CaCl_2$@UiO-66_38) was determined. This percentage corresponds to the molar ratio of 1:1.5 (Zr^{4+}:$CaCl_2$), which is similar to the initial value (1:1.6), confirming that spray drying is very efficient for incorporating $CaCl_2$ into the superstructures. Elemental mapping with energy dispersive X-ray spectrometry (EDX) was also performed on a single superstructure, which revealed a highly uniform distribution of Zr, Ca and Cl atoms (Figure 1c).

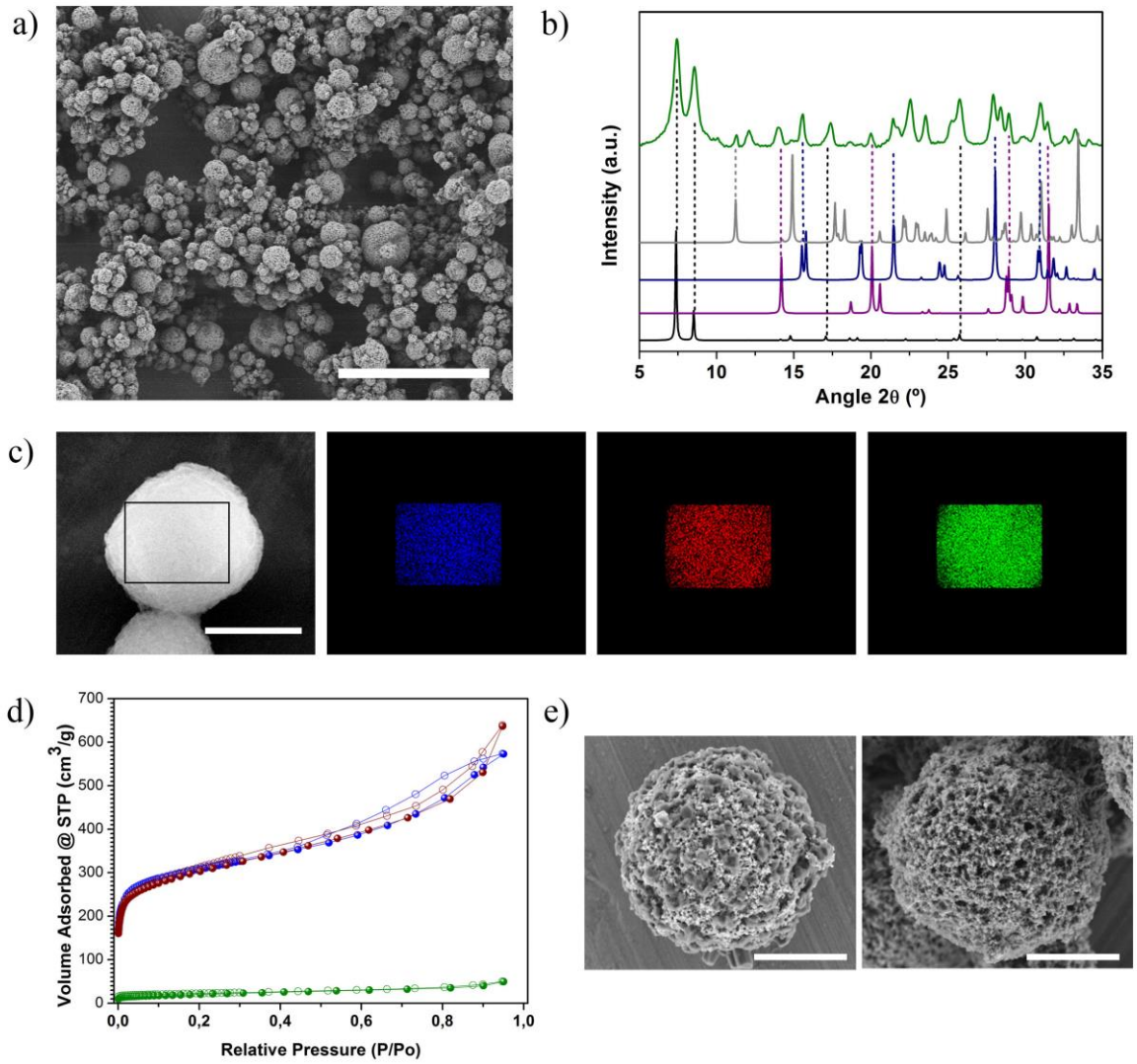

Figure 1. a) Representative FESEM image of microspherical $CaCl_2$@UiO-66_38 CSPMs. b) XRPD pattern of $CaCl_2$@UiO-66_38 powder (green), as compared to the corresponding simulated powder pattern of UiO-66 (black), $CaCl_2 \cdot 2H_2O$ (purple), $CaCl_2 \cdot 4H_2O\beta$ (grey) and $CaCl_2 \cdot 4H_2O\gamma$ (dark blue). c) Elemental mapping with EDX performed on a single spherical superstructure of $CaCl_2$@UiO-66_38, showing the homogeneous distribution of Zr (blue), Ca (red) and Cl (green). d) N_2 sorption isotherms of $CaCl_2$@UiO-66_38 (green), pristine UiO-66 (blue) and $CaCl_2$@UiO-66_38 after incubation in ethanol (red). e) FESEM images of microspherical $CaCl_2$@UiO-66_38

superstructures before (left) and after (right) incubation in ethanol. Scale bars: 20 μm (a), 5 μm (c) and 3 μm (e).

Nitrogen physical adsorption measurements on $CaCl_2$@UiO-66_38 (previously outgassed at 200 ºC) showed a measured Brunauer-Emmett-Teller (BET) surface area of *ca.* 70 $m^2\ g^{-1}$, which was very low compared to that of pristine UiO-66 superstructures that were also obtained by the spray-drying continuous-flow method (1106 $m^2\ g^{-1}$) (Figure 1d). We attribute this low microporosity to $CaCl_2$ particles, which are somehow blocking the access of N_2 molecules into the MOF micropores. This assumption was corroborated by removing the $CaCl_2$ from the $CaCl_2$@UiO-66_38 composites by incubating them in ethanol for 12 h at room temperature. Under these conditions, $CaCl_2$ was completely removed from the composites, as confirmed by the disappearance of the characteristic XRPD peaks of the $CaCl_2$ hydrates (Figure S1). Remarkably, the resulting UiO-66 superstructures showed a S_{BET} value that increased up to 1100 $m^2\ g^{-1}$ (Figure 1d). In addition, FESEM images of these UiO-66 superstructures revealed the formation of voids resulting from the dissolution of the $CaCl_2$ crystals (Figure 1e). The presence of these voids was in concordance with the higher increase in the N_2 adsorption in the range of pressures related to meso- and macroporosity as well as with the pore size distribution curve, in which the presence of mesopores with 14 nm in diameter was evidenced after removing $CaCl_2$ (Figure S2). In addition, the content of UiO-66 in the composite was estimated by weighting these superstructures, from which a UiO-66 content of 58 % w/w ($w_{UiO\text{-}66\text{-}1}/w_{CSPM}$) was determined. This percentage is similar to the expected 62 % if the $CaCl_2$@UiO-66_38 is composed of $CaCl_2$ and UiO-66. Altogether, these observations are important because they demonstrate that $CaCl_2$ particles are confined in the

micropores of UiO-66 and/or in the interparticular voids resulting from the assembly of UiO-66 nanocrystals in this class of superstructures.

Water sorption properties

Having determined the presence of both UiO-66 and $CaCl_2$ in $CaCl_2$@UiO-66_38, we then evaluated its water sorption properties. Water sorption isotherm of $CaCl_2$@UiO-66_38 (previously outgassed at 200 ºC) at 298 K showed two segments with steep increase in the water uptake (Figure 2a). These two steps were attributed to the formation of $CaCl_2 \cdot 0.33H_2O$ at a relative humidity (RH) of 3 % (water uptake of 0.15 $g_{water}\ g^{-1}_{CSPM}$) and to the further transformation of this hydrate to $CaCl_2 \cdot 2H_2O$ at RHs from 10 % to 16 % (water uptake of 0.33 $g_{water}\ g^{-1}_{CSPM}$).[7, 19] Then, the sorption curve ascended monotonically, indicating the formation of an aqueous solution of the salt and reaching a maximum water uptake of 1.93 $g_{water}\ g^{-1}_{CSPM}$ at a RH of 90 %.[7, 19] Interestingly, an hysteresis loop at low pressures ($P/P_0 = 0.10$-0.16) was observed in the desorption branch due to the structural changes in the transition from $CaCl_2 \cdot 2H_2O$ hydrate to $CaCl_2 \cdot 0.33H_2O$ hydrate, which is in agreement with other CSPMs based on mesoporous materials and salts crystals.[7, 20] Thus, we hypothesize that the water sorption takes place in the following steps: the anhydrous $CaCl_2$ particles confined in the micropores of UiO-66 and/or in the interparticular voids of superstructures adsorbs water and transforms to crystalline $CaCl_2 \cdot 0.33H_2O$; then, this hydrate adsorbs more water and is transformed to crystalline $CaCl_2 \cdot 2H_2O$; and finally, the salt is completely dissolved filling the pores and/or voids. Here, we also performed eight water sorption-desorption cycles by alternatively exposing $CaCl_2$@UiO-66_38 to humid (90 % RH) and dry (0 % RH) environments. Remarkably, the maximum uptake at 90 % RH (1.93 $g_{water}\ g^{-1}_{CSPM}$)

remained constant with the number of cycles, confirming the stability of this CSPM to water sorption/desorption processes (Figure 2c).

Water isotherm of $CaCl_2$@UiO-66_38 was compared with those of their individual components; that is, pristine UiO-66 superstructures and $CaCl_2$ (Figure 2a). As expected, $CaCl_2$@UiO-66_38 showed an intermediate adsorption capacity. Indeed, the adsorption was higher than UiO-66 superstructures (maximum water uptake = 0.61 $g_{water}\ g^{-1}_{UiO\text{-}66}$), demonstrating that $CaCl_2$ is very effective in increasing water uptake over the whole range of P/P_0, but lower than pristine $CaCl_2$ (maximum water uptake = 3.91 $g_{water}\ g^{-1}_{CaCl2}$). However, the main differences appeared when compared the aspect of the three samples exposed to a RH of 80 % at room temperature. Under these conditions, $CaCl_2$@UiO-66_38 and UiO-66 remained as solid adsorbents while $CaCl_2$ was dissolved with the water adsorbed due to the deliquescence effect (Figure 2d). Another difference was also found when desorption branches were compared. $CaCl_2$ retained around 0.70 $g_{water}\ g^{-1}_{CaCl2}$ (17.9 % of the total uptake) at a RH of ~0 %, whereas $CaCl_2$@UiO-66_38 retained only 0.06 $g_{water}\ g^{-1}_{CSPM}$ (3.1 % of the total uptake).

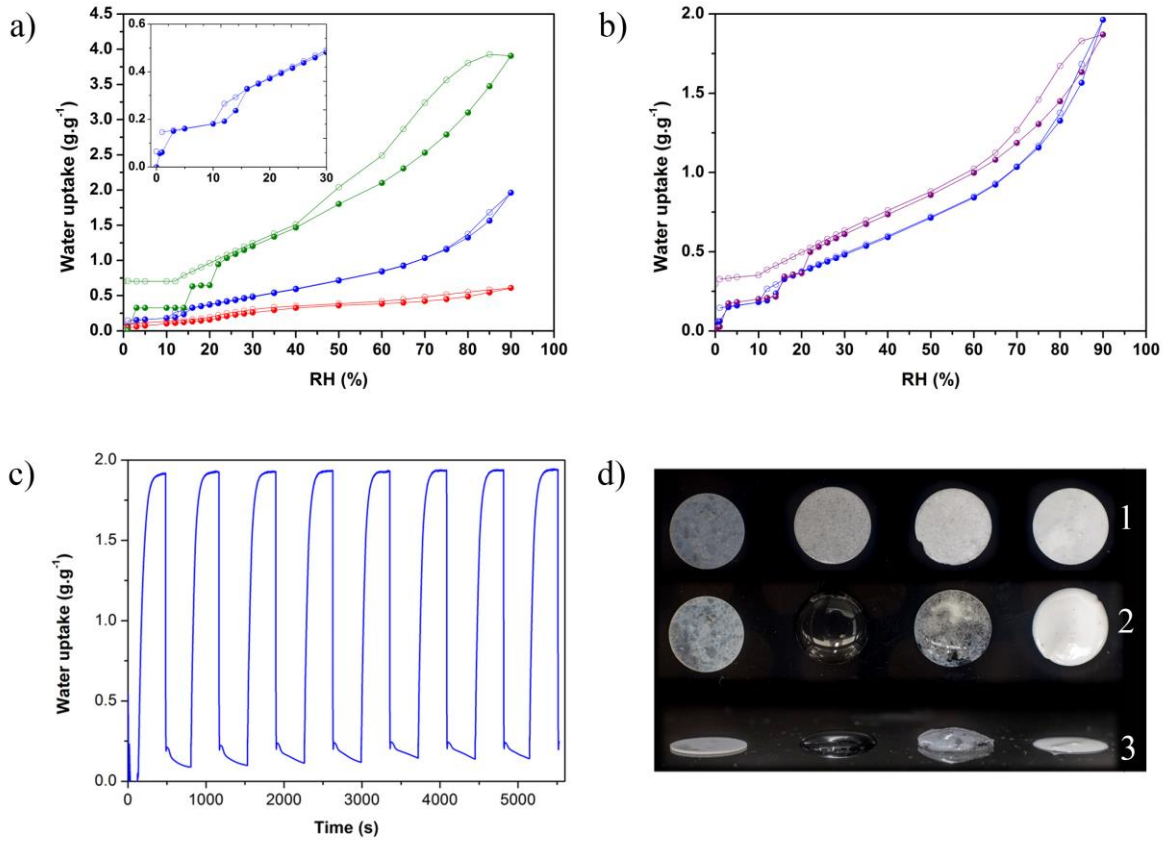

Figure 2. a) Water adsorption isotherms of UiO-66 (red), $CaCl_2$@UiO-66_38 (blue) and $CaCl_2$ (green). Insert shows water adsorption isotherm of $CaCl_2$@UiO-66_38 at low RHs. b) Water adsorption isotherms of $CaCl_2$@UiO-66_38 (blue) and the physical mixture (purple) (Adsorption: solid symbols; Desorption: open symbols). c) Adsorption and desorption cycles for $CaCl_2$@UiO-66_38. d) Photograph of the pellets of (from left to right) UiO-66, $CaCl_2 \cdot 2H_2O$, physical mixture and $CaCl_2$@UiO-66_38 before (1) and after (2 and 3) exposing them to a RH of 80 % at room temperature (2: top view, 3: lateral view).

To prove that the properties of $CaCl_2$@UiO-66_38 composite results from using the *in-situ* spray-drying synthesis and shaping methodology rather than simply mixing UiO-66 and $CaCl_2$, we also performed the water sorption measurement of a physical mixture of

$CaCl_2$ and UiO-66 superstructures (38 % and 62 % (*w/w*), respectively). The total water uptake of this mixture (1.86 $g_{water}\ g^{-1}_{mixture}$) was slightly lower than the composite uptake (Figure 2b), but properly matched with the percentage of contribution of the individual components. Again, the differences were the liquefaction of the $CaCl_2$ of this mixture when exposed to a RH of 80% at room temperature (Figure 2d), and a water retention of 0.30 $g_{water}\ g^{-1}_{mixture}$ (16.1% of the total uptake) at a RH of ~0 % (Figure 2b). This behavior is very similar to that found for the pristine $CaCl_2$, thereby confirming that a simple mixture is not enough for producing a composite that behaves as a solid adsorbent when adsorb water, as it does the spray-drying synthesized spherical superstructures.

Tuning the composition of $CaCl_2$

We then sought to assess the water sorption properties of $CaCl_2$@UiO-66 composites with diverse compositions, seeking to find an optimal $CaCl_2$/UiO-66 ratio in terms of maximum capacity of UiO-66 superstructures to host $CaCl_2$ while preventing its dissolution. Thus, we systematically synthesized a series of composites in which we increased the initial molar ratios of $CaCl_2$ from 1:2.6, 1:3.2, 1:4.8 to 1:6.4 (Zr^{4+}:$CaCl_2$). Again, the content of Ca in the composites was estimated by digesting the as-made samples (previously outgassed at 200 ºC under vacuum) in H_2SO_4 at 50 ºC and analysed by ICP-OES (Table S1). FESEM images revealed the formation of $CaCl_2$@UiO-66_X for the first three samples (where X = 50, 53 and 64 % w_{CaCl_2}/w_{CSPM}) in the form of spherical superstructures (Figures 3a-b and S3). However, $CaCl_2$@UiO-66_64 sample was discarded because it showed the presence of non-encapsulated $CaCl_2$ crystals together with the superstructures. In the case of a molar ratio of 1:6.4, crystalline spherical superstructures were not formed (Figure S3). For the first two compositions,

XRPD patterns confirmed the formation of UiO-66 and the presence of $CaCl_2$ hydrates (Figure 3c).

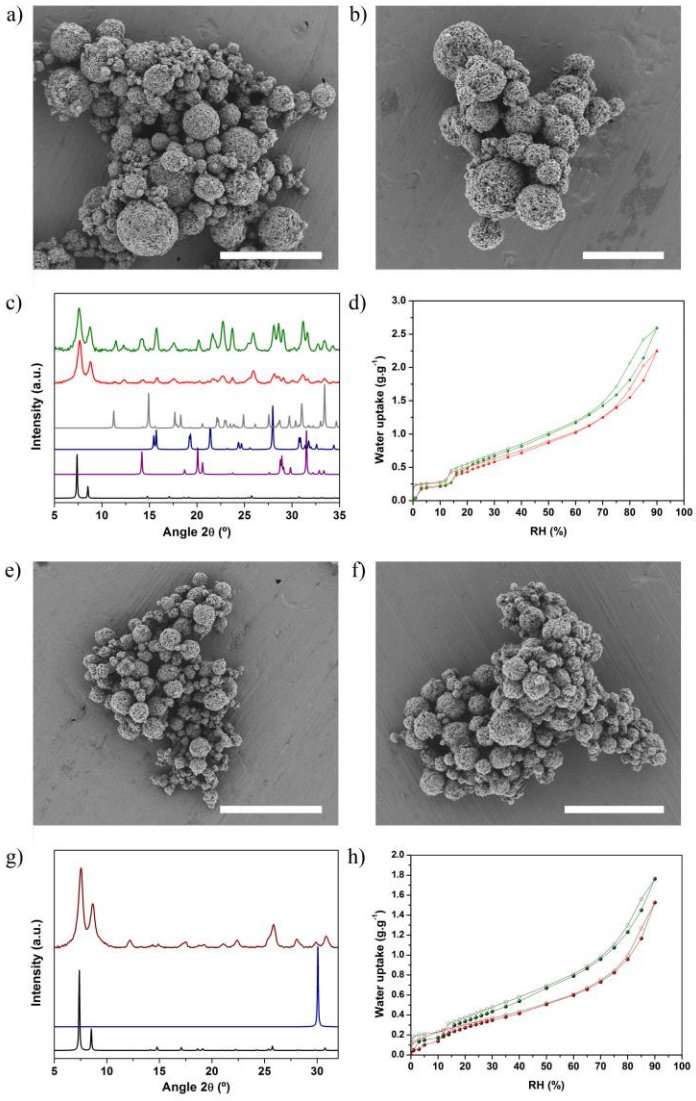

Figure 3. Representative FESEM images of a) $CaCl_2$@UiO-66_50, b) $CaCl_2$@UiO-66_53, e) LiCl@UiO-66_19 and f) $CaCl_2$@UiO-66-NH_2_38. c) XRPD diffractograms of $CaCl_2$@UiO-66_50 (red) and $CaCl_2$@UiO-66_53 (green), as compared to the simulated powder pattern for UiO-66 (black), $CaCl_2 \cdot 2H_2O$ (purple), $CaCl_2 \cdot 4H_2O\gamma$ (dark blue) and $CaCl_2 \cdot 4H_2O\beta$ (grey). d) Water adsorption isotherms of $CaCl_2$@UiO-66_50 (red) and $CaCl_2$@UiO-66_53 (green) at 25 ºC. g) XRPD diffractograms of LiCl@UiO-66_19, as compared to the simulated powder pattern for UiO-66 (black) and LiCl (dark

blue). h) Water adsorption isotherms of LiCl@UiO-66_19 (dark red) and $CaCl_2$@UiO-66-NH_2_38 (dark green). Scale bars: 20 μm (a, e) and 10 μm (b and f).

To examine the water adsorption properties of the $CaCl_2$@UiO-66_50 and $CaCl_2$@UiO-66_53 CSPMs, water adsorption isotherms were measured at 298 K (Figure 3d). All resulting isotherms displayed the characteristic steps related to the formation of $CaCl_2 \cdot 0.33H_2O$ and $CaCl_2 \cdot 2H_2O$ hydrates, and the hysteresis loop in the desorption branch. The maximum uptake of the composites was 2.24 $g_{water}\ g^{-1}_{CSPM}$ ($CaCl_2$@UiO-66_50) and 2.59 $g_{water}\ g^{-1}_{CSPM}$ ($CaCl_2$@UiO-66_53) at RH of 90%. As expected, a greater amount of $CaCl_2$ let to achieve a higher water uptake. As well, a higher amount of $CaCl_2$ resulted in higher water retention values at a RH of ~0 %, as evidenced by the water retentions of 0.17 $g_{water}\ g^{-1}_{mixture}$ (7.6 % of the total uptake) for $CaCl_2$@UiO-66_50 and of 0.20 $g_{water}\ g^{-1}_{mixture}$ (7.7 % of the total uptake) for $CaCl_2$@UiO-66_53; in comparison to that observed in $CaCl_2$@UiO-66_38 (3.1 % of the total uptake).

Synthesis of LiCl@UiO-66 and $CaCl_2$@UiO-66-NH_2 composites

To demonstrate the generality of our approach, we used the spray-drying technique to synthesize other Salt@MOF CSPMs substituting the inorganic salt and the MOF. Thus, we prepared LiCl@UiO-66 and $CaCl_2$@UiO-66-NH_2 using the same conditions as for $CaCl_2$@UiO-66_38, except that instead of $CaCl_2$ in the first case and UiO-66 in the second case, we used LiCl and UiO-66-NH_2, respectively. In both cases, pure microspherical superstructures were obtained, as confirmed by FESEM and XRPD (Figure 3e-g and S4). The content of Li and Ca was also estimated by ICP-OES, from which a LiCl content of 19 % w/w in LiCl@UiO-66_19 and a $CaCl_2$ content of 38 % *w/w* in $CaCl_2$@UiO-66-NH_2_38 were determined. Here, water sorption measurements at 298 K showed that LiCl@UiO-66_19 exhibits a high water uptake of 1.53 $g_{water}\ g^{-}$

$^{1}_{CSPM}$ at a RH of 90% and a water retention of 0.07 g_{water} g^{-1}_{CSPM} (4.6 % of the total uptake) during desorption (Figure 3h). On the other hand, $CaCl_2$@UiO-66-NH_2_38 showed a maximum uptake of 1.76 g_{water} g^{-1}_{CSPM}, which is lower compared with its analogue based on UiO-66, and it retained 0.12 g_{water} g^{-1}_{CSPM} (6.8 % of the total uptake) of water at a RH of 0%, which doubles that of its UiO-66 analogue.

Thermal batteries application

Figure S5 summarizes the working capacity for all prepared materials and the most promising UiO-66-based CSPMs were tested as potential adsorbents in thermal batteries and adsorption heat pumps applications according to their working capacity (ΔW). Among them, thermal batteries have been recently explored as an alternative to the traditional air conditioning systems in electric vehicles. Traditionally, the climate control system is based in a vapour compression system where the compressor is driven by an electric battery with high power consumption, producing a decrease in the efficiency of the electric vehicle. Thermal batteries are based in a sorption and desorption cycles where large amounts of energy can be reversibly stored for provide heating and cooling efficiently. As consequence, the consumption of electric power decreases and the driving range of the electric vehicle increases [2c, 21]

To evaluate our CSPMs as adsorbents for thermal batteries, we selected $CaCl_2$@UiO-66_38 because it has the higher working capacity (Δw = 0.12 g_{water} g^{-1}_{CSPM}) at P/P_0 = 0.1 (Figure 2a). It is important to highlight here that water adsorption is desirable at a relative pressure of 0.1 to reduce the need of using compressors in the system.[15]

Once $CaCl_2$@UiO-66_38 was selected, the heat storage capacity (C_{HS}) was estimated according to the Equation (1)[2b].

$$C_{HS} = \frac{\Delta H_{ads} \cdot \Delta w}{M_w} \qquad (1)$$

where M_w is the water molar weight and ΔH_{ads} is the heat of adsorption. ΔH_{ads} of $CaCl_2$@UiO-66_38 was calculated using water isotherms collected at different temperatures (25, 40 and 50 ºC; Figure 4a), and then adjust to the Clausius-Clapeyron Equation (2).[22]

$$\Delta H_{ads} = -R\, ln\left(\frac{P_2}{P_1}\right)\frac{T_1 \cdot T_2}{T_2 - T_1} \qquad (2)$$

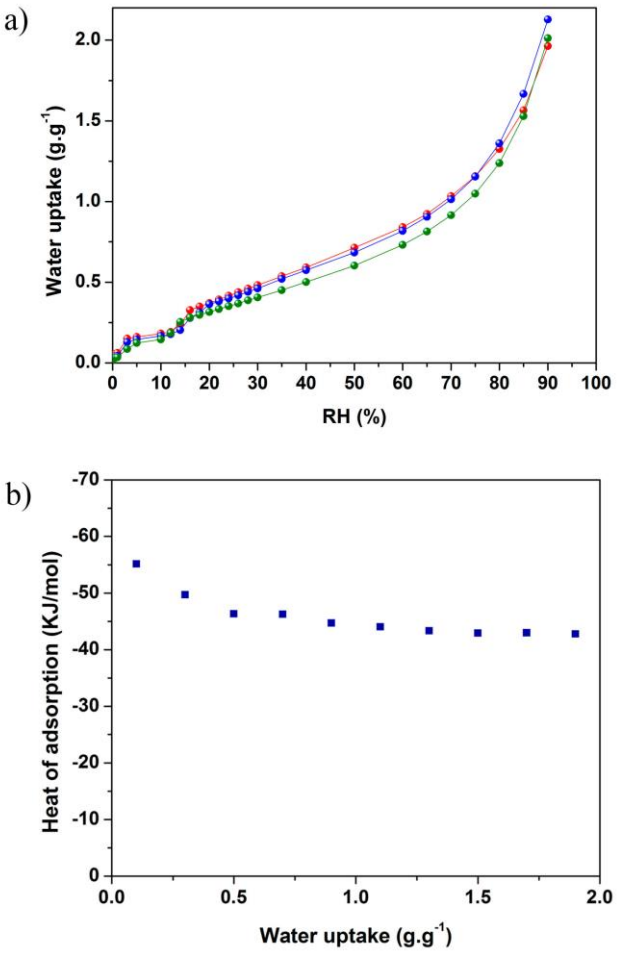

Figure 4. a) Water adsorption isotherms of $CaCl_2$@UiO-66_38 at 30 ºC (red), 40 ºC (blue) and 50 ºC (green). b) Heat of adsorption of $CaCl_2$@UiO-66_38.

It was found that ΔH_{ads} values decrease as water uptakes increase (from *ca.* 55 kJ mol^{-1} to *ca.* 43 kJ mol^{-1}; Figure 4b), and that ΔH_{ads} was 55 kJ mol^{-1} for a working capacity of 0.12 g_{water} g^{-1}_{CSPM}. These values are in agreement with the initial formation of the $CaCl_2$ hydrate, where the water molecules are stronger bounded and then, a decrease to 43 kJ mol^{-1} is due to the formation of an aqueous solution of $CaCl_2$.[23]

Finally, a C_{HS} value of 367 kJ kg^{-1} was determined using Equation (1). According to primary technical targets for thermal batteries,[24] the minimum heat storage capacity should be 2.5 kWh. This means that 24.5 Kg of $CaCl_2$@UiO-66_38 will be required to achieve this capacity, which is less than the total weight of the system (35 Kg) suggested by U.S. Department of Energy (DOE).[24]

Adsorption chillers application

To evaluate our CSPMs as adsorbents for adsorption chillers, we selected $CaCl_2$@UiO-66_53 because it had the higher working capacity at P/P_0 = 0.3, which is a typical value for practical applications.[2a] In order to describe the performance and the efficiency of this system, the specific cooling power (SCP), an isosteric cycle diagram and the coefficient of performance (COP) were determined.

The average specific cooling power (SCP) describes the effectiveness of the system during the cooling process and is defined as the ratio of cooling power per mass of adsorbent per cycle time according to Equation (3).[2b]

$$SCP = \frac{\Delta H_{vap} \cdot \Delta w \cdot 0.8}{M_w \, (\tau_{0.8ads} + \tau_{0.8ads})} \quad (3)$$

where ΔH_{vap} is the water enthalpy of evaporation, Δw is the working capacity of the $CaCl_2$@UiO-66_53/H_2O pair, M_w is the water molar weight, and $\tau_{0.8ads}$ and $\tau_{0.8des}$ are the adsorption and desorption times when the conversion q = 0.8 (Figure 5).

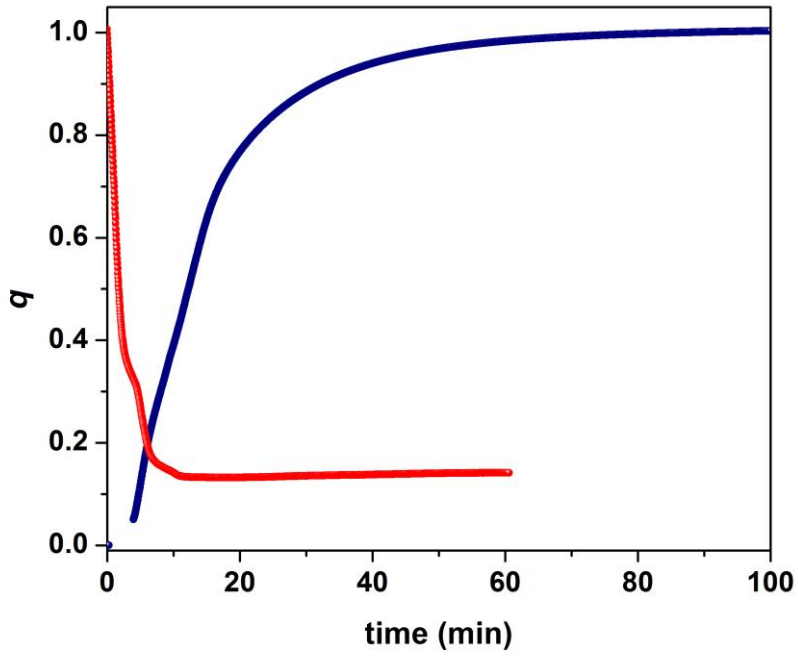

Figure 5. Kinetics of water adsorption of $CaCl_2$@UiO-66_53 at T = 303 K and P = 1.24 kPa (blue) and desorption at T = 370 K and P = 5.4 kPa (red).

An isosteric cycle diagram of an adsorption air conditioning cycle was analyzed to determine Δw and the desorption temperature (T_{des}) (Figure 6). This diagram was calculated using the water adsorption isobars at vapor pressures of 0.7, 1.2, 2.4, 3.7, 4.2

and 5.6 kPa (Figure S6), and fixing the operational temperatures of the cycle to a temperature of evaporation (T_{ev}) of 283 K and to a temperature of adsorption and condensation ($T_{ad} = T_{con}$) of 303 K. In the isobaric adsorption (step IV-I), the water was adsorbed in the composite reaching a maximum uptake of 0.60 $g_{water}\ g^{-1}_{CSPM}$. Then, during the isosteric heating (I-II), the $CaCl_2$@UiO-66_53 was fully saturated and the pressure increased from 1.2 kPa to 4.2 kPa by increasing the temperature from 303 K to 317 K without desorption. In the isobaric desorption (II-III), the heating was continued and desorption process was started until reached a T_{des} of 370 K, in which the water uptake was minimal. Finally, in the isosteric cooling, decreasing the temperature reduced the pressure, and the composite was regenerated. In this cycle, Δw depends on the T_{des} (Figure S7), where Δw increases from 0.3 $g_{water}\ g^{-1}_{CSPM}$ at T_{des} = 330 K to 0.56 $g_{water}\ g^{-1}_{CSPM}$ at T_{des} = 370 K. These values are higher compared to traditional adsorbents like zeolites, silica gel and other CSPMs (Table 1), and are in the range of some reported MOFs (*e.g.* NH_2-MIL-12: 0.39 $g_{water}\ g_{MOF}^{-1}$; CPO-27(Ni): 0.41 $g_{water}\ g_{MOF}^{-1}$; MOF-841: 0.44 $g_{water}\ g_{MOF}^{-1}$) [2b, 15, 25]

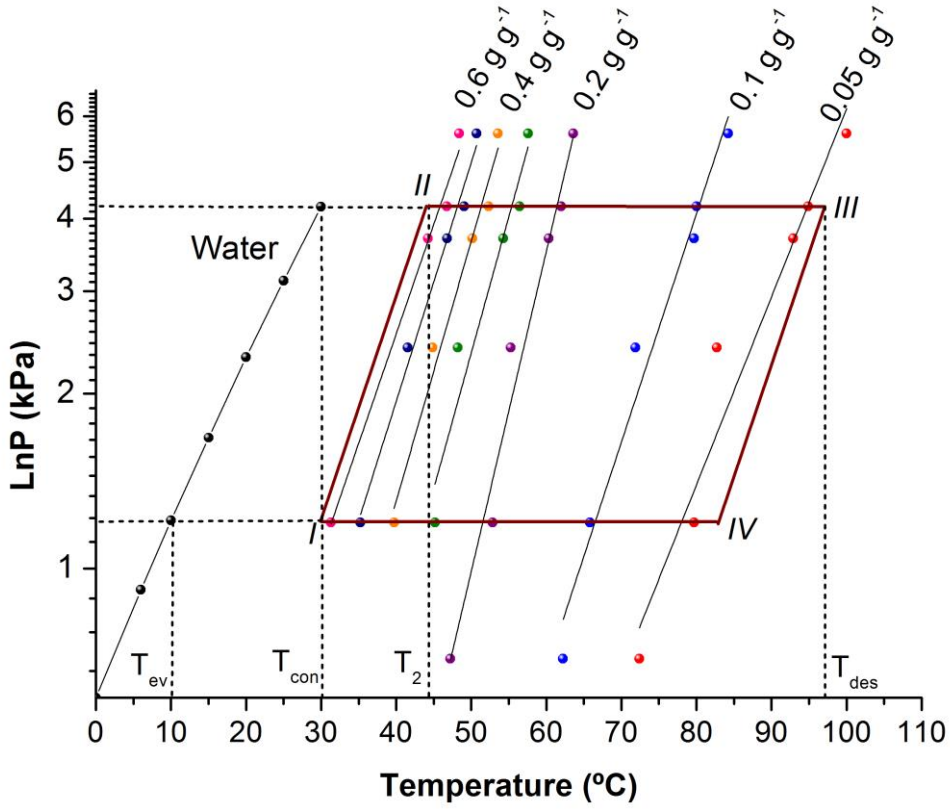

Figure 6. Isosteric cycle diagram for $CaCl_2$@UiO-66_53/water working pair calculated for a air cooling cycle.

The adsorption and desorption times were calculated from the kinetic curves of water adsorption and desorption (Figure 5), which were performed under the standard T_{ad} = 303 k, P_{ad} = 1.24 kPa and P_{des} = 5.4 kPa conditions and the determined T_{des} = 370 K. From these curves, we found that $\tau_{0.8ads}$ and $\tau_{0.8des}$ were 1320 s and 380 s, respectively. Finally, a SCP value of 631 W kg^{-1} was calculated according to Equation 3.[2b]

In an adsorption air conditioning system, COP is a factor that helps describing the energetic efficiency. COP is defined as the useful output energy divided by the energy required as input.[26] Thus, COP is the ratio of the vaporization heat (Q_{ev}) and regeneration heat (Q_{reg}) according to Equation (4).[12c]

$$COP = \frac{Q_{ev}}{Q_{reg}} \qquad (4)$$

Here, the vaporization (Q_{ev}) and regeneration (Q_{reg}) heats were calculated from Equations 5-8:

$$Q_{ev} = \frac{\Delta H_{vap}(T_{ev}) \cdot \rho \cdot m \cdot \Delta w}{M_w} \qquad (5)$$

where ρ is the water density and *m* is the amount of $CaCl_2$@UiO-66_53 used in the cycle.

$$Q_{reg} = Q_{I-II} + Q_{II-III} \qquad (6)$$

$$Q_{I-II} = \int_{T_{con}}^{T_2} {C_p}^{cspm}(T)dT + \int_{T_{con}}^{T_2} \rho \cdot W_{max} {C_p}^{water}(T)dT \qquad (7)$$

$$Q_{II-III} = \int_{T_2}^{T_{des}} {C_p}^{cspm}(T)dT + \int_{T_{con}}^{T_2} \rho \cdot \frac{W_{max} + W_{min}}{2} \cdot {C_p}^{water}(T)dT$$

$$- \frac{1}{M_w} \int_{W_{min}}^{W_{max}} \rho \cdot \Delta H_{ads}(W)dW \qquad (8)$$

where C_p^{cspm} is the heat capacity of $CaCl_2$@UiO-66_53 and C_p^{water} is the heat capacity of water.

Thus, the sorption heat (ΔH_{ads}) of the working pair $CaCl_2$@UiO-66_53/water and the heat capacity (C_p) of $CaCl_2$@UiO-66_53 were initially determined. The ΔH_{ads} was calculated using the Clausius-Clapeyron equation and water isotherms at two different temperatures (25 and 40 ºC) (Figure S8). As seen in the previous section, the ΔH_{ads} decreased as water uptake increased (from *ca.* 52 kJ mol^{-1} to *ca.* 41 kJ mol^{-1}; Figure S9). Afterwards, the C_p of $CaCl_2$@UiO-66_53 was determined from DSC analysis, from which an average C_p of 0.76 J g^{-1} K^{-1} was calculated over the temperature range of 303-353 K (Figure S10).

Once we determined these parameters, COP was calculated as a function of T_{des} (Figure 7). For a T_{des} from 330 to 383 K, a COP value of 0.83 remained almost constant, meaning that 0.83 J of cold can be generated from 1 J of waste heat.

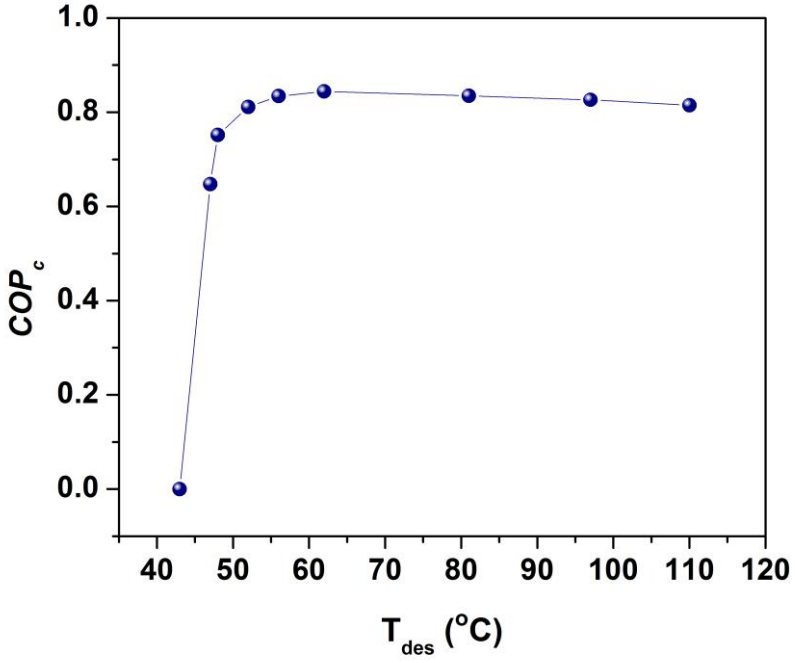

Figure 7. Coefficient of performance (COP) as a function of desorption temperature for the $CaCl_2$@UiO-66_53/Water working pair.

Table 1. Water loading, regeneration temperature, COPc, and SCP for selected materials compared with $CaCl_2$@UiO-66_53 composite.

Adsorbent	Water loading [$g \cdot g^{-1}$]	Regeneration temperature [°C]	COP_c	SCP [$W \cdot kg^{-1}$]	Reference
$CaCl_2$@UiO-66_53	0.60	57-110	0.83	631	This work
Silica gel	-	85	0.37	63.4	[27]
Activated carbon	0.19	115	0.37	65	[28]

Zeolite 13-X	0.25	310	0.38	25.7	[29]
AQSOA-FAM-Z02 (ALPO-34)	0.28	90	025-0.3	260	[30]
SWS-8L ($Ca(NO_3)_2$@mesoporous silica)	-	90-95	0.18-0.31	190-389	[31]
SWS-9V ($LiNO_3$@vermeculite)	0.4	70	0.59	96	[32]
$CaCl_2$@Silica-Carbon	0.43	115	0.7	378	[28]
NH_2-MIL-125	0.42	90	0.8	3200	[2b]
CPO-27(Ni)	0.41	130	0.45	440	[25]

Finally, we also studied the multiple adsorption-desorption cycles under operational conditions for air conditioning systems (P = 2.36 kPa, and T_{ads} = 303 K and T_{des} = 383 K). Figure 8 shows six consecutive cycles in which, after the first three cycles, a very small decrease in the water uptake (from 0.63 to 0.61 g g^{-1}) was observed. Then, water uptake becomes stable, without a significant loss of adsorption and desorption capacities during the remaining cycles.

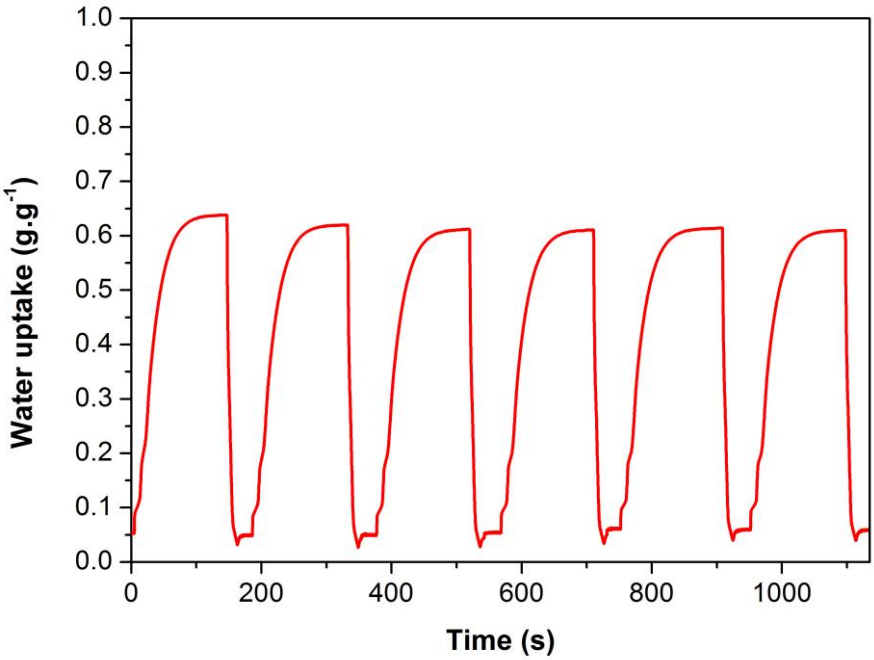

Figure 8. Adsorption-desorption cycles under operational conditions for air conditioning systems (P = 2.36 kPa, and T_{ads} = 303 K and T_{des} = 383 K) for $CaCl_2$@UiO-66_53.

CONCLUSION

In conclusion, we have reported a continuous and fast methodology for the fabrication of MOF-based CSPM materials using the spray drying continuous flow method, which enables the simultaneous synthesis and shaping of microspherical MOF superstructures while confining the salts. This method also enables tuning the composition of the resulting CSPMs. We have demonstrated the applicability of these MOF-based CSPMs for potential applications in thermal batteries and refrigerator systems. For the first application, we have shown that $CaCl_2$@UiO-66_38 exhibits a C_{HS} of 367 kJ kg^{-1}; which fulfills the conditions suggested by the U.S. Department of Energy to use it in thermal batteries. For the latter application, the working pair $CaCl_2$@UiO-66_53/water displays a high capacity and energetic efficiency, exhibiting a COP of 0.83. This value is higher

than traditional working pairs based on silica and zeolites and others CSPMs, which exhibit COP values from 0.3 to 0.6, (*e.g.* silica gel: 0.3; zeolite-NaX: 0.38; natural zeolite: 0.34; and LiCl@Silica: 0.41)[4] and it is comparable with the most energy efficient MOFs (NH_2-MIL-125: 0.8; CAU-3: 0.7; MOF-841: 0.8) reported so far.[2b, 12c, 26] We believe that this methodology will facilitate the synthesis of other CSPMs, in which the nature of the MOF and the salt can be changed, as well as of new composites resulting from the combination of MOFs with other nanomaterials such as inorganic nanoparticles or graphene.

EXPERIMENTAL SECTION

Materials and methods: Zirconium chloride, calcium chloride, lithium chloride, terephthalic acid and 2-aminoterephthalic acid were purchased from Sigma Aldrich. Dimethylformamide was obtained from Fisher Chemical. All the reagents were used without further purification. Deionised water, obtained with a Milli-Q® system (18.2 MΩ·cm), was used in all reactions.

X-ray powder diffraction (XRPD) patterns were collected on an X'Pert PRO MPDP analytical diffractometer (Panalytical) at 45 kV, 40 mA using CuKα radiation (λ = 1.5419 Å). Field-Emission Scanning Electron Microscopy (FESEM) images were collected on a FEI Magellan 400L scanning electron microscope at an acceleration voltage of 2.0 KV and FEI Quanta 650F scanning electron microscope with Energy-dispersive X-ray spectroscopy (EDX) Inca 250 SSD XMax20 at an acceleration voltage of 20.0 KV, using aluminium as support. ICP-OES measurements were performed using a Perkin Elmer Optima 4300DV after HF digestion. Prior to the ICP analysis, samples were degassed under vacuum at 200 ºC. Volumetric N_2 sorption isotherms were collected at 77 K using an AutosorbIQ-AG analyser (Quantachrome

Instruments). Gravimetric water vapor sorption isotherms were measured using a DVS vacuum instrument (Surface Measurement Systems Ltd). The weight of the dried powder (~ 20 mg) was constantly monitored with a high resolution microbalance (± 0.1 μg) and recorded at 25 ºC, 35 ºC and 45 ºC (± 0.2 °C) under pure water vapor pressures. The kinetics curves of water vapor adsorption were obtained measuring real time mass change. The isobars were recorded at different temperatures from 110 ºC to 30 ºC a fixed pressure of 0.7, 1.2, 2.4, 3.7, 4.2 and 5.6 kPa. Prior to the sorption experiments, samples were degassed inside the chamber under vacuum at 200 ºC for 6 h. The heat capacity measurements were performed on a Differential Scanning Calorimeter (Mettler Toledo). The heating rate used was 10 ºC min^{-1} from 10 ºC to 90 ºC and sapphire was used as a reference material.

Spray-drying continuous flow-assisted synthesis of UiO-66 and UiO-66-NH_2 superstructures.

UiO-66 and UiO-66-NH_2 superstructures were synthesized according to the method reported recently.[17b] In a typical synthesis, a solution 0.1 M of $ZrCl_4$ and 0.1 M of the organic ligand in 15 ml of a mixture of DMF and H_2O (5.48:1) was injected into the coil flow reactor (Pyrex tube, inner diameter: 3 mm) at a feed rate of 2.4 ml min^{-1} and at a T_1 of 115 ºC. The resulting pre-heated solution was then spray-dried at a T_2 of 180 ºC and a flow rate of 336 ml min^{-1} using a Dryer B-290 Mini Spray (BUCHI Labortechnik; spray cap: 0.5-mm-hole). Finally, the collected solid was dispersed in DMF at room temperature, stirred overnight and precipitated by centrifugation. This process was repeated twice with ethanol instead of DMF. The final product was dried for 12 h at 80 ºC.

Spray-drying continuous flow-assisted synthesis of UiO-66-based CSPMs.

A 15 ml solution containing 0.1 M of $ZrCl_4$, 0.1 M of terephthalic acid and a solution of $CaCl_2 \cdot H_2O$ (at the concentration of 0.16. 0.26, 0.32, 0.48 and 0.64 M) or LiCl (at the concentration of 0.16) in a mixture of DMF and H_2O (5.48:1) was injected into the coil flow reactor (Pyrex tube, inner diameter: 3 mm) at a feed rate of 2.4 ml min^{-1} and at a T_1 of 115 ºC. The resulting pre-heated solution was then spray-dried at a T_2 of 180 ºC and a flow rate of 336 ml min^{-1} using a Dryer B-290 Mini Spray (BUCHI Labortechnik; spray cap: 0.5-mm-hole), collecting a white solid.

Spray-drying continuous flow-assisted synthesis of $CaCl_2$@UiO-66-NH_2.

A 15 ml solution containing 0.1 M of $ZrCl_4$, 0.1 M of 2-amino-terephthalic acid and 0.16 M of $CaCl_2 \cdot H_2O$ in a mixture of DMF and H_2O (5.48:1) was injected into the coil flow reactor (Pyrex tube, inner diameter: 3 mm) at a feed rate of 2.4 ml min^{-1} and at a T_1 of 115 ºC. The resulting pre-heated solution was then spray-dried at a T_2 of 180 ºC and a flow rate of 336 ml min^{-1} using a Dryer B-290 Mini Spray (BUCHI Labortechnik; spray cap: 0.5-mm-hole), collecting a yellow solid.

Supporting Information

Supporting Information is available from the Wiley Online Library or from the author.

Acknowledgements

This work was supported by the Spanish MINECO (projects PN MAT2015-65354-C2-1-R), the Catalan AGAUR (project 2014 SGR 80), the ERC under the EU FP7 (ERC-Co 615954),

and European Union's Horizon 2020 research and innovation programme under grant agreement No 685727. ICN2 acknowledges support of the Spanish MINECO through the Severo Ochoa Centers of Excellence Programme (Grant SEV-2013-0295). We thank Dr. Vincent Guillerm for the photographic work.

REFERENCES

[1] P. Tatsidjodoung, N. Le Pierrès, L. Luo, *Renewable Sustainable Energy Rev.* **2013**, *18*, 327.

[2] a) J. Canivet, A. Fateeva, Y. Guo, B. Coasne, D. Farrusseng, *Chem. Soc. Rev.* **2014**, *43*, 5594; b) L. G. Gordeeva, M. V. Solovyeva, Y. I. Aristov, *Energy* **2016**, *100*, 18; c) S. Narayanan, X. Li, S. Yang, H. Kim, A. Umans, I. S. McKay, E. N. Wang, *Appl. Energy* **2015**, *149*, 104.

[3] S. K. Henninger, F. P. Schmidt, H. M. Henning, *Appl. Therm. Eng.* **2010**, *30*, 1692.

[4] a) L. G. Gordeeva, Y. I. Aristov, *Int. J. Low-Carbon Tech.* **2012**, *7*, 288; b) H. Demir, M. Mobedi, S. Ülkü, *Renewable Sustainable Energy Rev.* **2008**, *12*, 2381.

[5] Y. I. Aristov, *Appl. Therm. Eng.* **2013**, *50*, 1610.

[6] X. J. Zhang, L. M. Qiu, *Energy Convers. Manage.* **2007**, *48*, 320.

[7] Y. Yuan, H. Zhang, F. Yang, N. Zhang, X. Cao, *Renewable Sustainable Energy Rev.* **2016**, *54*, 761.

[8] a) Y. Tashiro, M. Kubo, Y. Katsumi, T. Meguro, K. Komeya, *J. Mater. Sci.* **2004**, *39*, 1315; b) F. Meunier, *Appl. Therm. Eng.* **2013**, *61*, 830; c) L. Bonaccorsi, L. Calabrese, A. Freni, E. Proverbio, G. Restuccia, *Appl. Therm. Eng.* **2013**, *50*, 1590.

[9] a) W. Wang, L. Wu, Z. Li, Y. Fang, J. Ding, J. Xiao, *Drying Technol.* **2013**, *31*, 1334; b) X. Wei, W. Wang, J. Xiao, L. Zhang, H. Chen, J. Ding, *Chem. Eng. J.* **2013**, *228*, 1133.

[10] a) L. Wang, D. Zhu, Y. Tan, *Adsorption* **1999**, *5*, 279; b) S. Szarzynski, Y. Feng, M. Pons, *Int. J. Refrig.* **1997**, *20*, 390.

[11] a) H. Furukawa, N. Ko, Y. B. Go, N. Aratani, S. B. Choi, E. Choi, A. Ö. Yazaydin, R. Q. Snurr, M. O'Keeffe, J. Kim, O. M. Yaghi, *Science* **2010**, *329*, 424; b) Y.-K. Seo, J. W. Yoon, J. S. Lee, U. H. Lee, Y. K. Hwang, C.-H. Jun, P. Horcajada, C. Serre, J.-S. Chang, *Microporous Mesoporous Mater.* **2012**, *157*, 137.

[12] a) J. Ehrenmann, S. K. Henninger, C. Janiak, *Eur. J. Inorg. Chem.* **2011**, *2011*, 471; b) A. Khutia, H. U. Rammelberg, T. Schmidt, S. Henninger, C. Janiak, *Chem. Mater.* **2013**, *25*, 790; c) M. F. de Lange, K. J. F. M. Verouden, T. J. H. Vlugt, J. Gascon, F. Kapteijn, *Chem. Rev.* **2015**, *115*, 12205; d) A. Cadiau, J. S. Lee, D. Damasceno Borges, P. Fabry, T. Devic, M. T. Wharmby, C. Martineau, D. Foucher, F. Taulelle, C.-H. Jun, Y. K. Hwang, N. Stock, M. F. De Lange, F. Kapteijn, J. Gascon, G. Maurin, J.-S. Chang, C. Serre, *Adv. Mater.* **2015**, *27*, 4775.

[13] a) A. Mallick, T. Kundu, R. Banerjee, *Chem. Commun.* **2012**, *48*, 8829; b) S. C. Sahoo, T. Kundu, R. Banerjee, *J. Am. Chem. Soc.* **2011**, *133*, 17950; c) R. M. P. Colodrero, P. Olivera-Pastor, E. R. Losilla, D. Hernández-Alonso, M. A. G. Aranda, L. Leon-Reina, J. Rius, K. D. Demadis, B. Moreau, D. Villemin, M. Palomino, F. Rey, A. Cabeza, *Inorg. Chem.* **2012**, *51*, 7689.

[14] P. Guo, A. G. Wong-Foy, A. J. Matzger, *Langmuir* **2014**, *30*, 1921.

[15] H. Furukawa, F. Gandara, Y. B. Zhang, J. Jiang, W. L. Queen, M. R. Hudson, O. M. Yaghi, *J. Am. Chem. Soc.* **2014**, *136*, 4369.

[16] J. Yan, Y. Yu, C. Ma, J. Xiao, Q. Xia, Y. Li, Z. Li, *Appl. Therm. Eng.* **2015**, *84*, 118.

[17] a) A. Carné-Sánchez, I. Imaz, M. Cano-Sarabia, D. Maspoch, *Nat Chem* **2013**, *5*, 203; b) L. Garzon-Tovar, M. Cano-Sarabia, A. Carne-Sanchez, C. Carbonell, I. Imaz, D. Maspoch, *React. Chem. Eng.* **2016**, *1*, 533.

[18] M. Kim, S. M. Cohen, *CrystEngComm* **2012**, *14*, 4096.

[19] a) ; b) I. Glaznev, I. Ponomarenko, S. Kirik, Y. Aristov, *Int. J. Refrig.* **2011**, *34*, 1244.

[20] Y. I. Aristov, G. Restuccia, G. Cacciola, V. N. Parmon, *Appl. Therm. Eng.* **2002**, *22*, 191.

[21] Y. S. Nam, R. Enright, S. Maroo, E. N. Wang, S. Narayanan, I. S. McKay, *US 20130192281 A1*, **2013**.

[22] J. Rouquerol, F. Rouquerol, P. Llewellyn, G. Maurin, K. S. W. Sing, *Adsorption by Powders and Porous Solids: Principles, Methodology and Applications*, Elsevier Science, **2013**.

[23] Y. I. Aristov, M. M. Tokarev, G. Cacciola, G. Restuccia, *React. Kinet. Catal. Lett.* **1996**, *59*, 325.

[24] Advanced Research Projects Agency-DOE, HEATS Program Overview, https://arpa-e.energy.gov/sites/default/files/documents/files/HEATS_ProgramOverview.pdf, October 27, 2016.

[25] B. Shi, R. Al-Dadah, S. Mahmoud, A. Elsayed, E. Elsayed, *Appl. Therm. Eng.* **2016**, *106*, 325.

[26] M. F. de Lange, B. L. van Velzen, C. P. Ottevanger, K. J. F. M. Verouden, L.-C. Lin, T. J. H. Vlugt, J. Gascon, F. Kapteijn, *Langmuir* **2015**, *31*, 12783.

[27] D. C. Wang, Z. Z. Xia, J. Y. Wu, R. Z. Wang, H. Zhai, W. D. Dou, *Int. J. Refrig.* **2005**, *28*, 1073.

[28] C. Y. Tso, C. Y. H. Chao, *Int. J. Refrig.* **2012**, *35*, 1626.

[29] L. Z. Zhang, *Appl. Therm. Eng.* **2000**, *20*, 103.

[30] S. Vasta, A. Freni, A. Sapienza, F. Costa, G. Restuccia, *Int. J. Refrig.* **2012**, *35*, 701.

[31] A. Freni, A. Sapienza, I. S. Glaznev, Y. I. Aristov, G. Restuccia, *Int. J. Refrig.* **2012**, *35*, 518.

[32] A. Sapienza, I. S. Glaznev, S. Santamaria, A. Freni, Y. I. Aristov, *Appl. Therm. Eng.* **2012**, *32*, 141.